

Non-isothermal phase-field modelling with thermocapillary convection: Laser-written in-plane SiGe heterostructures for photonic applications

Ozan Aktas (✉ O.Aktas@soton.ac.uk)

University of Southampton <https://orcid.org/0000-0002-2255-7761>

Yuji Yamamoto

IHP-Leibniz-Institut für Innovative Mikroelektronik

Mehmet Kaynak

IHP-Leibniz-Institut für Innovative Mikroelektronik

Anna Peacock

University of Southampton

Article

Keywords: non-isothermal phase-field modelling, thermocapillary convection, SiGe heterostructures

Posted Date: November 5th, 2020

DOI: <https://doi.org/10.21203/rs.3.rs-81573/v1>

License:  This work is licensed under a Creative Commons Attribution 4.0 International License.

[Read Full License](#)

Version of Record: A version of this preprint was published on June 11th, 2021. See the published version at <https://doi.org/10.1038/s42005-021-00632-1>.

1 Non-isothermal phase-field modelling with thermocapillary convection: 2 Laser-written in-plane SiGe heterostructures for photonic applications

3
4 Ozan Aktas^{1,*}, Yuji Yamamoto², Mehmet Kaynak², and Anna C. Peacock¹

5
6 ¹Optoelectronics Research Centre, University of Southampton, Southampton, SO17 1BJ, UK

7
8 ²IHP-Leibniz-Institut für Innovative Mikroelektronik, Im Technologiepark 25, 15236 Frankfurt
9 (Oder), Germany

10
11 *Corresponding author, e-mail: O.Aktas@soton.ac.uk

13 ABSTRACT

14 Advanced solid-state device applications, including semiconductor lasers, waveguide Bragg
15 gratings, and modulators, require nanoscale engineering of the electronic bandgap and
16 refractive index. Heterostructures, which are semiconductor structures with a position-
17 dependent chemical composition, are building blocks of these devices, enabling control over
18 the carriers and light. However, existing epitaxial growth methods are limited to fabrication of
19 vertical heterostructures between dissimilar semiconductors successively grown layer by layer.
20 Here, we report the use of three dimensional (3D) finite-element-method (FEM)-based non-
21 isothermal phase-field modelling with thermocapillary convection to investigate a new concept
22 for laser inscription of in-plane longitudinal and transverse heterostructures within silicon-
23 germanium ($\text{Si}_{1-x}\text{Ge}_x$) alloy thin films. The modelling has been supported by exploratory
24 experimental work using $\text{Si}_{0.5}\text{Ge}_{0.5}$ layers epitaxially grown on a silicon substrates. Results of
25 the phase-field simulations reveal that various in-plane SiGe heterostructures and superlattices
26 can be fabricated by controlling the steady-state and transient effects of the laser scanning on
27 phase segregation through modulation of the laser power, scan speed and beam position during
28 solidification of the SiGe epilayers. Optical simulations are used to demonstrate the potential
29 for two new photonic devices based on in-plane SiGe heterostructures written at different scan
30 speeds (1-200 mm s^{-1}): (i) graded-index waveguides with Ge-rich (70%) cores, and (ii)
31 waveguide Bragg gratings with nanoscale periods ($\Lambda=100\text{-}500$ nm). Periodic heterostructure

32 formation via sub-millisecond modulation of the laser processing parameters opens a route for
33 post-growth fabrication of in-plane quantum wells and superlattices in semiconductor alloy
34 epilayers.

35 INTRODUCTION

36 Modern-day applications of microelectronics, optoelectronics and photonics have become
37 undoubtedly possible with the technological advancements in material growth and formation
38 of interfaces between different materials. For example, the development of semiconductor
39 heterostructures, quantum wells, and superlattices, which provide confinement for light and
40 carriers via spatially engineered refractive index and bandgap profiles, has enabled the
41 fabrication of various devices such as heterojunction bipolar transistors (HBT), double
42 heterojunction lasers (DHL), quantum cascade lasers (QCL), distributed Bragg reflectors
43 (DBR), semiconductor saturable absorber mirrors (SESAM), photodetectors, and modulators.¹⁻

44 ⁴ Methods commonly used to grow epitaxial layers of semiconductors are molecular beam
45 epitaxy (MBE) and derivatives of chemical vapour deposition (CVD), which allow for material
46 growth with atomic precision and control.^{5,6} However, these methods implement a layer-by-
47 layer growth approach; therefore, they can only be used to fabricate vertical heterostructures
48 and superlattices,⁷ which are limited in total thickness ($< 5 \mu\text{m}$) due to the constraint of lattice
49 matching and strain issues. Recently, fabrication of lateral and axial heterostructures have been
50 demonstrated in semiconductor alloys of nanoribbons,^{8,9} and nanowires,^{10,11} respectively, by
51 switching the precursors during material growth on planar substrates. However, a versatile
52 strategy to fabricate in-plane heterostructures, quantum wells and superlattices within
53 semiconductor alloy epilayers has yet to be demonstrated.

54 As an alternative to heterostructure formation via successive epitaxial growth, post-
55 process approaches such as thermally-induced phase segregation have been applied to induce
56 axial and lateral heterostructures in initially homogeneous alloys of nanowires,¹² and
57 monolayers,¹³ respectively. Similar manifestations of phase segregation resulting in quasi-

58 regular in-plane heterostructures have also been observed in semiconductor superlattices due to
59 the strain-induced lateral compositional self-modulation,¹⁴ and directionally solidified alloys
60 where banding occurs due to oscillations of the solidification speed near the instability regime.¹⁵
61 However, because of their spontaneous and elusive nature, it is challenging to control these
62 effects to form heterostructures within semiconductor alloy thin films. Generally, phase
63 segregation is an undesired phenomenon even for epitaxial growth of vertical heterostructures
64 in semiconductor alloy epilayers. This is particularly true for SiGe alloys,¹⁶ which have a large
65 miscibility gap between the liquidus and solidus curves in the equilibrium phase diagram.

66 For stable growth from a melted SiGe alloy where phase segregation results in a Ge-
67 rich liquid phase, solidification speeds have to be smaller than a critical speed, which depends
68 on the local temperature gradient and thermophysical properties of the alloy. Otherwise,
69 constitutional undercooling can emerge ahead of the solid/liquid interface, breaking its
70 stability.¹⁷ Consequently, the interface instability results in cellular or faceted structures during
71 bulk crystal growth,¹⁸⁻²⁰ and dendritic structures during laser annealing of SiGe thin films on
72 glass substrates,²¹⁻²³ leading to a random spatial redistribution of the initial homogenous
73 composition. In order to exploit heat-induced phase segregation for the fabrication of regular
74 in-plane heterostructures with well-defined morphologies, cellular or dendritic solidification of
75 alloy thin films needs to be avoided by ensuring either low growth speeds or high temperature
76 gradients at the liquid/solid interface. However, low solidification speeds, on the order of 10
77 $\mu\text{m s}^{-1}$ to allow for stable growth, are impractical in terms of process time. Another alternative
78 is the application of non-conventional thermal sources, like lasers, to post-process
79 semiconductor alloy thin films grown on substrates with high thermal conductivities.^{24,25} Such
80 methods allow for achieving extremely high temperature gradients (10^9 K m^{-1}) and cooling rates
81 (10^5 K s^{-1}), which are required to ensure the stability of the solid/liquid interface. Recently, by
82 using laser processing of amorphous SiGe thin films deposited on silicon substrates, the
83 fabrication of non-dendritic SiGe microstripes was demonstrated with steady-state

84 compositional profiles that can be tuned by applying different constant scan speeds in the range
85 of 0.1-100 mm s⁻¹.²⁶ Additionally, it is known from classical theory of solidification that
86 transient effects such as acceleration of the liquid/solid interface can be used to form localized
87 compositional heterostructures,²⁷ and this was recently demonstrated by laser processing of low
88 Ge-content SiGe core silica clad fibers.²⁸

89 Over the past two decades, phase-field models have been extensively applied to study
90 the formation of cellular and dendritic nanostructures during solidification of alloys,²⁹⁻³² where
91 an order parameter $\phi(r, t)$ is used to track the liquid/solid interface. Here we extend these
92 studies to show that it can also be exploited for modelling non-dendritic solidification of laser-
93 melted semiconductor alloys. A 3D FEM-based phase-field model was used to investigate non-
94 dendritic non-isothermal solidification with thermocapillary convection, and transient and
95 steady-state effects on phase segregation at the moving liquid/solid interface. The simulation
96 results are supported with experimental data, which were obtained by optical microscopy and
97 scanning transmission electron microscopy (STEM) with energy-dispersive X-ray spectroscopy
98 (EDX), using Si_{0.5}Ge_{0.5} alloy thin films epitaxially grown on silicon substrates. Based on this,
99 we introduce a concept for post-process laser-writing of in-plane heterostructures and
100 superlattices in semiconductor alloy epilayers. Our work focuses on SiGe alloy epilayers
101 because of the increasing interest in Ge/SiGe heterostructures in micro/nanostructures,³³ and
102 their tantalizing prospect for quantum cascade lasers³ and parabolic quantum wells,³⁴ etc.
103 However, our method can be applied to pseudo-binary alloys of other materials, such as ternary
104 semiconductors (Al_xGa_{1-x}As) with isomorphous phase diagrams similar to that of SiGe. The
105 potential to use our method for photonic applications is demonstrated via FEM-based optical
106 simulations of two new devices based on laser-written in-plane SiGe heterostructures: (i)
107 graded-index waveguides for mid-infrared photonic applications, and (ii) waveguide Bragg
108 gratings for wavelength filtering in the mid-infrared spectrum.

109

110 RESULTS

111 Calculation of the equilibrium phase diagram for SiGe alloys

112 We followed a thermodynamically consistent phase-field approach to derive a convection-
113 diffusion-segregation equation and a heat transport equation, using the molar Gibbs free energy
114 of SiGe alloys. By calculating the equilibrium phase diagram of SiGe alloys and fitting it to the
115 experimental phase diagram data, we estimated the parameters in the molar Gibbs free energy
116 $F(\phi, T, x)$, which is given at a constant pressure for a regular solution model of alloys by,³⁵

$$117 F = (1 - x)F_{Si}(\phi, T) + xF_{Ge}(\phi, T) + RT[(1 - x) \ln(1 - x) + x \ln(x)] + w(\phi)x(1 - x), \quad (1)$$

118 where x is the molar fraction of Ge, R is the ideal gas constant, T is the temperature, ϕ is the
119 phase-field representing the solid ($\phi = 0$) and liquid ($\phi = 1$) phases. $F_{Si}(\phi, T)$ and $F_{Ge}(\phi, T)$
120 are the Gibbs free energies in units of J mol^{-1} for pure silicon and germanium, respectively. The
121 molar Gibbs free energy for a pure element A (Si or Ge) is given by

$$122 F_A(\phi, T) = H_A g(\phi) + L_A \left(1 - \frac{T}{T_m^A}\right) p(\phi) + F_{A, \text{Solid}}, \quad (2)$$

123 where H_A is the height of the energy barrier between the liquid and solid phases at the melting
124 temperature T_m^A ; L_A is the latent heat of melting; $g(\phi) = \phi^2(1 - \phi)^2$ is the double-well
125 potential function with minima at $\phi = 0$ and $\phi = 1$; and $p(\phi) = \phi^2(3 - 2\phi)$ is an
126 interpolating function, which satisfies $p(\phi = 0) = 0$ and $p(\phi = 1) = 1$. The height of the
127 energy barrier H_A is assumed to be the same for Si and Ge, due to the similar atomic properties.
128 $F_{A, \text{Solid}}$ is the Gibbs free energy of the solid pure element A, which is assumed to be zero as a
129 reference for the Gibbs free energy. The last term in Eq. (1) is the molar excess Gibbs free
130 energy for the regular solution, which is proportional to the parameter $w(\phi)$ given by

$$131 w(\phi) = w_S(1 - \phi) + w_L \phi, \quad (3)$$

132 where w_S and w_L are regular solution parameters corresponding to solid and liquid phases of
133 the SiGe alloy, respectively.

134 The chemical potentials μ for silicon and germanium can be calculated from the molar
 135 Gibbs energy $F(\phi, T, x)$ in Eq. (1) as:

$$136 \quad \mu_{Si}(\phi, T, x) = F - x \frac{\partial F}{\partial x} = w(\phi)x^2 + F_{Si}(\phi, T) + RT \ln(1 - x), \quad (4)$$

$$137 \quad \mu_{Ge}(\phi, T, x) = F + (1 - x) \frac{\partial F}{\partial x} = w(\phi)(1 - x)^2 + F_{Ge}(\phi, T) + RT \ln(x). \quad (5)$$

138 In the case of phase coexistence at thermal equilibrium, the chemical potential for each element
 139 in the solid (S) and liquid (L) solutions are equal, and given by

$$140 \quad \mu_{Si}^S(\phi = 0, T, x_S) = \mu_{Si}^L(\phi = 1, T, x_L), \quad (6)$$

$$141 \quad \mu_{Ge}^S(\phi = 0, T, x_S) = \mu_{Ge}^L(\phi = 1, T, x_L), \quad (7)$$

142 where x_S and x_L are the Ge molar fractions in the solid and liquid solutions of $\text{Si}_{1-x}\text{Ge}_x$,
 143 respectively. By using Eqs. (2-5), Eqs. (6) and (7) can be rewritten explicitly in terms of the
 144 regular solution parameters, latent heats of melting, and melting temperatures of the alloy
 145 elements,³⁶ as given below

$$146 \quad \ln \frac{1 - x_S}{1 - x_L} = \frac{L_{Si}}{R} \left(\frac{1}{T} - \frac{1}{T_m^{Si}} \right) + \frac{1}{RT} (w_L x_L^2 - w_S x_S^2), \quad (8)$$

$$147 \quad \ln \frac{x_S}{x_L} = \frac{L_{Ge}}{R} \left(\frac{1}{T} - \frac{1}{T_m^{Ge}} \right) + \frac{1}{RT} [w_L (1 - x_L)^2 - w_S (1 - x_S)^2], \quad (9)$$

148 which are implicit analytic expressions for the liquidus and solidus lines in the phase diagram
 149 of SiGe, corresponding to $x_L(T)$ and $x_S(T)$, respectively. The best fitting parameters for the
 150 experimental phase diagram of SiGe alloys, as shown in Supplementary Figure S1, were found
 151 to be $T_m^{Si} = 1687$ K, $L_{Si}/R = 6040$ K, $T_m^{Ge} = 1211$ K, $L_{Ge}/R = 4441$ K, $w_S/R = 450$ K
 152 and $w_L/R = 800$ K.

153

154 **Non-isothermal phase-field formulation of convection-diffusion-segregation and heat**
 155 **transport equations with laser-induced thermocapillary effect**

156 To describe the laser heating process, a convection-diffusion-segregation equation needs to be
 157 formulated incorporating phase segregation in the laser-melted SiGe epilayers, as well as the
 158 convection in the molten pool, which is driven mainly by the thermocapillary (Marangoni)
 159 effect. For a non-isothermal derivation, we postulate an entropy functional S defined by the
 160 integral of the entropy density $s(e, \phi, x)$ over the whole SiGe thin film volume, as given by,

$$161 \quad S = \int \left[s(e, \phi, x) - \frac{\varepsilon_\phi^2}{2} |\nabla \phi|^2 \right] dV, \quad (10)$$

162 where e is the energy density, $\phi(\vec{r}, t)$ is the phase-field parameter representing the solid
 163 domains and laser-induced traveling molten zone in the $\text{Si}_{1-x}\text{Ge}_x$ thin film, and ε_ϕ is a constant
 164 related to the thickness and energy of the solid/liquid interface. Time-dependent equations,
 165 which ensure the entropy functional S always increases according to the laws of
 166 thermodynamics,³⁷ can be derived for the Ge molar fraction and energy density as

$$167 \quad \frac{\partial x}{\partial t} = -\nabla \cdot \left[M_x \nabla \left(\frac{\partial S}{\partial x} \right) \right] = \nabla \cdot \left[M_x \nabla \left(\frac{1}{T} \frac{\partial f}{\partial x} \right) \right], \quad (11)$$

$$168 \quad \frac{\partial e}{\partial t} = -\nabla \cdot \left[M_e \nabla \left(\frac{\partial S}{\partial e} \right) \right] = -\nabla \cdot \left[M_e \nabla \left(\frac{1}{T} \right) \right], \quad (12)$$

169 where M_e and M_x are positive mobility parameters related to the thermal conductivity and
 170 diffusion constant, respectively, T is the spatial distribution of temperature, and $f(\phi, T, x)$ is
 171 the Gibbs free energy density in units of J m^{-3} , which is derived from the molar Gibbs free
 172 energy F given in Eq. (1), divided by the molar volume V_m of the alloy:

$$173 \quad f(\phi, T, x) = \frac{F(\phi, T, x)}{V_m}. \quad (13)$$

174 The laser-processed SiGe thin films were treated as a highly viscous liquid with a
 175 dynamic viscosity $\mu(\phi)$ varying by several orders of magnitude between the solid region
 176 ($\mu_S=1.0\times 10^3 \text{ N m}^{-1} \text{ s}$) and laser-melted liquid region ($\mu_L=0.8\times 10^{-3} \text{ N m}^{-1} \text{ s}$), which is given as

$$177 \quad \mu(\phi) = \mu_L p(\phi) + \mu_S(1 - p(\phi)), \quad (14)$$

178 where $p(\phi)$ is the interpolation function. The surface tension σ for the liquid SiGe alloy, which
 179 was estimated using the surface tensions of liquid Si and Ge,³⁸ is assumed to be a linear function
 180 of temperature T as

$$181 \quad \sigma(T) = 0.653 (N m^{-1}) - 10^{-4}(N m^{-1} K^{-1})[T - T_m], \quad (15)$$

182 where T_m is the melting temperature of the alloy. To describe fluid motion due to the
 183 thermocapillary effect in the laser-induced molten pool, Navier-Stokes equations were solved
 184 assuming a laminar incompressible flow ($\nabla \cdot \vec{u} = 0$) with a velocity field of \vec{u} .³⁹ By adding a
 185 conservative convection term on the left hand side of Eq. (11), a convection-diffusion-
 186 segregation equation is finally derived as,

$$187 \quad \frac{\partial x}{\partial t} + \nabla \cdot (\vec{u}x) = \nabla \cdot \left\{ M_x \left[\frac{\partial}{\partial x} \left(\frac{1}{T} \frac{\partial f}{\partial x} \right) \nabla x + \frac{\partial}{\partial \phi} \left(\frac{1}{T} \frac{\partial f}{\partial x} \right) \nabla \phi + \frac{\partial}{\partial T} \left(\frac{1}{T} \frac{\partial f}{\partial x} \right) \nabla T \right] \right\}. \quad (16)$$

188 Here, $\partial f / \partial x$ is calculated from Eqs. (1) and (13) as

$$189 \quad \frac{\partial f}{\partial x} = \frac{1}{V_m} \left\{ \left[L_{Ge} \left(1 - \frac{T}{T_m^{Ge}} \right) - L_{Si} \left(1 - \frac{T}{T_m^{Si}} \right) \right] p(\phi) + RT \ln \left(\frac{x}{1-x} \right) + w(\phi)(1-2x) \right\}, \quad (17)$$

190 To ensure a composition independent diffusion coefficient D , the mobility M_x is taken as

$$191 \quad M_x = \frac{D(\phi)T}{\partial^2 f(\phi, T, x) / \partial^2 x} = \frac{V_m D(\phi) T (1-x)x}{RT - 2x(1-x)w(\phi)}, \quad (18)$$

192 where the phase-dependent diffusion coefficient is

$$193 \quad D(\phi) = D_S(1 - \phi) + D_L \phi. \quad (19)$$

194 The diffusion coefficients in the liquid and solid SiGe phases are taken as $D_L = 3.0 \times 10^{-8} \text{ m}^2 \text{ s}^{-1}$
 195 and $D_S = 10^{-16} \text{ m}^2 \text{ s}^{-1}$, respectively. When $\nabla\phi = 0$ and $\nabla T = 0$, the standard diffusion equation
 196 is obtained, as the Ge concentration C is related to the Ge molar fraction x by $C = x/V_m$.

197 For derivation of a heat transport equation, the energy density of a partially melted alloy
 198 at constant pressure and volume can be written in terms of the phase-field ϕ as,⁴⁰

$$199 \quad e = \rho[h_{p,s}(1 - \phi) + h_{p,l}\phi], \quad (20)$$

200 where ρ is the density of the SiGe alloy, which is assumed to be constant, and $h_{p,s}$ and $h_{p,l}$, are
 201 the specific enthalpies of the solid and liquid phases, respectively. By inserting Eq. (20) into
 202 Eq. (12), we obtain

$$203 \quad \rho \left[\frac{dh_{p,s}}{dT} (1 - \phi) + \frac{dh_{p,l}}{dT} \phi \right] \frac{dT}{dt} + \rho (h_{p,l} - h_{p,s}) \frac{d\phi}{dT} \frac{dT}{dt} = \nabla \cdot \frac{M_e}{T^2} \nabla T, \quad (21)$$

204 which can be recast into the conventional heat transport equation as

$$205 \quad \rho \left[c_{p,s}(1 - \phi) + c_{p,l}\phi + L \frac{d\phi}{dT} \right] \frac{dT}{dt} = \nabla \cdot k \nabla T. \quad (22)$$

206 Here, $k = M_e/T^2$ is the thermal conductivity, and $c_{p,s}$ and $c_{p,l}$ are the specific heat capacity of the
 207 solid and liquid phases, respectively. The terms in the square parenthesis can be defined as an
 208 apparent heat capacity c_p

$$209 \quad c_p = c_{p,s}(1 - \phi) + c_{p,l}\phi + L \frac{d\phi}{dT}, \quad (23)$$

210 where $L = \rho(h_{p,l} - h_{p,s})$ is the latent heat of melting for the SiGe alloy, which is estimated as
 211 $L = xL_{Ge} + (1 - x)L_{Si}$ using Vegard's law. By including the effect of the fluid flow with
 212 velocity field of \vec{u} , and a heat source, the final form of the heat transport equation in Eq. (22)
 213 can be written as

$$214 \quad \rho c_p \left[\frac{dT}{dt} + \vec{u} \cdot \nabla T \right] = \nabla \cdot k \nabla T + Q. \quad (24)$$

215 Here, the external heat source Q , due to the volumetric absorption of the Gaussian laser beam,
 216 is given by Beer–Lambert law in terms of absorption coefficient α and laser intensity I as

219 $Q = \alpha I(x, y, z) = \alpha \frac{2(1-R)P_0}{\pi r_0^2} e^{-2(x(t)^2+y^2)/r_0^2} e^{\alpha z},$ (25)

217 where $R=0.4$ is reflection coefficient, P_0 is the optical power, r_0 is the beam radius, and $x(t) =$
 218 vt is given in terms of the time t and constant scan speed v .

220 During laser scanning, the morphology of the liquid/solid interface, represented by the
 221 phase-field ϕ , is dictated by the laser beam characteristics such as power, radius, scan speed,
 222 and wavelength, which determines the absorption coefficient. Additionally, the thickness of the
 223 solid/liquid interface doesn't have a unique value, because it is determined by the temperature
 224 range (mushy zone) between the liquidus and solidus curves, and depends on the local
 225 temperature gradient ∇T and composition. For example, the smallest value for the thickness of
 226 the mushy interface occurs at the bottom of the molten zone, due to the highest temperature
 227 gradient. Therefore, to reduce the number of differential equations for the simulations of non-
 228 dendritic alloy solidification, we assume that the phase-field $\phi(T)$ is an explicit function of the
 229 temperature T , smoothly rising from $\phi = 0$ (solid) to $\phi = 1$ (liquid) between the solidus
 230 temperature T_S and liquidus temperature T_L , which were calculated for the initial Ge molar
 231 fraction of $x_0=0.5$. The temperature derivative of ϕ in Eq. (23) is defined by a unit area
 232 parabolic function, which moderates the capture and release of the latent heat as

233 $\frac{d\phi}{dT} = \left\{ \begin{array}{l} 0, \quad T < T_m - \Delta T/2 \\ \frac{3}{2\Delta T} \left(1 - \frac{(T - T_m)^2}{(\Delta T/2)^2} \right), \quad T_m - \Delta T/2 < T < T_m + \Delta T/2 \\ 0, \quad T > T_m + \Delta T/2 \end{array} \right\},$ (26)

234 where $T_m = (T_S + T_L)/2$ is the melting temperature of the alloy, and $\Delta T = (T_L - T_S)/2$ is the
 235 temperature range for the mushy zone. We also assumed that the thermal properties of the
 236 $\text{Si}_{0.5}\text{Ge}_{0.5}$ alloy such as the melting temperature and thermal conductivity are determined by the
 237 initial composition $x_0=0.5$, and stay constant during the simulations.

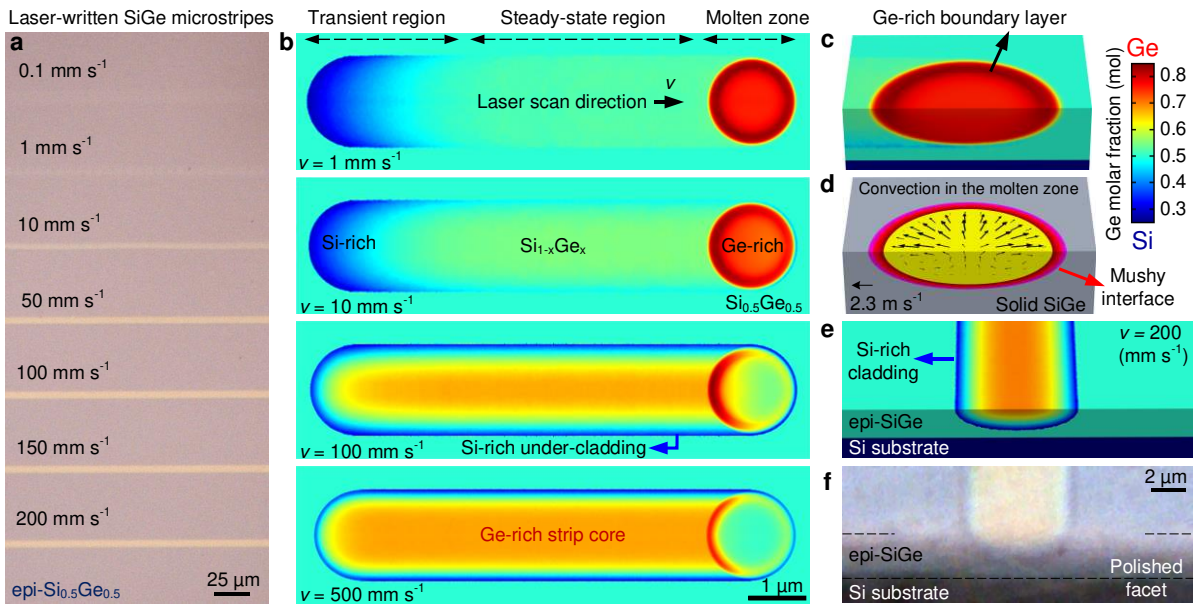
238

239 **Laser writing of in-plane longitudinal SiGe heterostructures with tunable**
240 **compositionally-graded profiles at various constant scan speeds**

241 We begin our investigations of laser-driven heterostructure formation with some preliminary
242 experimental work, by applying laser processing on homogenous SiGe epilayers with a
243 thickness of 575 nm and a Ge concentration of 50%. The $\text{Si}_{0.5}\text{Ge}_{0.5}$ epilayers were epitaxially-
244 grown on (100) silicon substrates by reduced pressure chemical vapour deposition (RPCVD).¹⁶
245 As a thermal source, we used a continuous wave (CW) laser operating at 532 nm and an
246 experimental setup schematically shown in Supplementary [Figure S2](#). The laser beam with a
247 power of 3 W was focused to a spot with a diameter of 5 μm on the surface of the $\text{Si}_{0.5}\text{Ge}_{0.5}$
248 epilayer by a 10 \times microscope objective. Scanning the stage under the fixed laser beam produces
249 a traveling molten zone, where phase segregation occurs at the liquid/solid interface. Depending
250 on the scan speed, the laser-driven liquid/solid interface produces microstripes solidified with
251 varying Ge compositions on the top surface, as shown in the optical microscope image in [Figure](#)
252 [1\(a\)](#). The laser-written SiGe microstripes for the low scan speeds of 0.1 and 1 mm s^{-1} are barely
253 visible; however, wider microstripes emerge with a yellowish colour as the scan speed increases
254 and Ge accumulates on the surface.

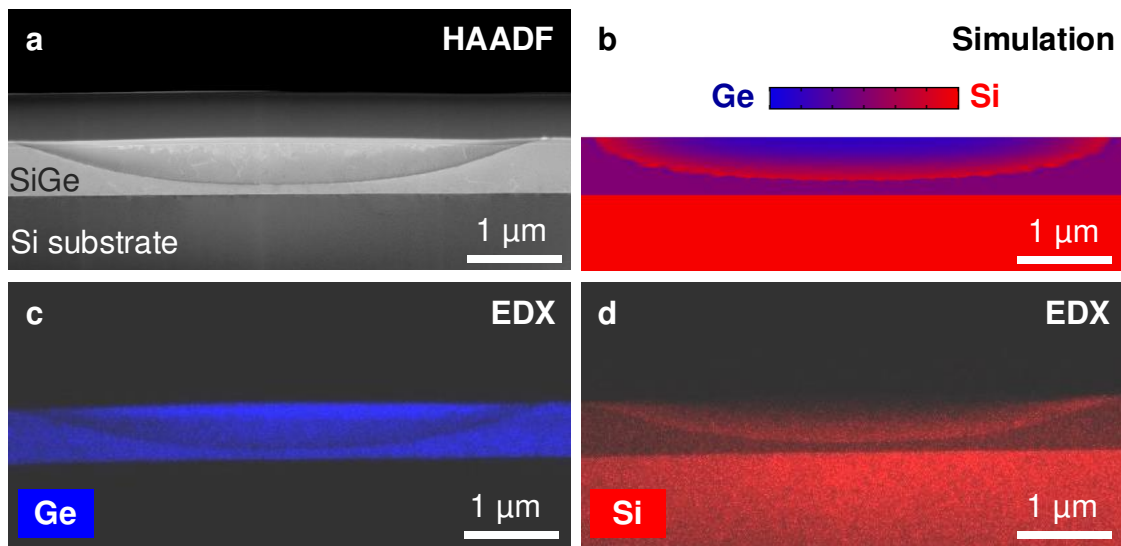
255 We then carried out 3D FEM-based non-isothermal phase-field simulations to compare
256 with the experimental results, conducted at the same power with different constant scan speeds.
257 Buoyancy-driven convection within the laser-induced molten pool was neglected because the
258 highest temperature is reached on the top surface, where the fluid with the lowest density
259 already resides. On the other hand, the thermocapillary effect, which is due to the temperature
260 dependent surface tension, is the dominant driving force for the convection, which can result in
261 fluid flows with high speeds in a range of 1-10 m s^{-1} for semiconductors melted by lasers.^{41,42}
262 To understand the effect of the thermocapillary convection on the distribution of composition
263 within the molten zone, Navier-Stokes equations were solved concurrently with [Eqs. \(16\)](#) and
264 [\(24\)](#). To reduce the simulation volume and computational cost, we chose a beam spot size of 2

265 μm and a scan range of $10\ \mu\text{m}$, which are smaller in size compared to the experimental
 266 parameters. The other parameters used in the simulations were: optical power of 200 mW, scan
 267 speeds in the range of $1\text{-}500\ \text{mm s}^{-1}$, and a $\text{Si}_{0.5}\text{Ge}_{0.5}$ epilayer (epi-SiGe) with a thickness of 500
 268 nm. The values used for the material and thermal properties of the SiGe alloys were taken from
 269 the literature (Supplementary Table 1). Further details regarding the implementation of the
 270 FEM-based phase-field simulations are given in the Methods.



271
 272 **Fig. 1: Laser writing of in-plane longitudinal SiGe heterostructures via scan-speed-**
 273 **dependent spatial redistribution of Ge.** a) Optical microscope image showing laser-written
 274 microstripes on a $\text{Si}_{0.5}\text{Ge}_{0.5}$ thin film epitaxially grown on Si substrates, for scan speeds in the
 275 range of $0.1\text{-}200\ \text{mm s}^{-1}$. b) Results of FEM-based non-isothermal phase-field simulations for
 276 laser-driven phase segregation are given as composition colour maps showing the Ge molar
 277 fraction $x(\vec{r})$ for the short transient (blue) and indefinitely-long steady-state regions (yellow-
 278 orange) solidified behind the laser-induced molten zone (red) traveling at a constant scan speed
 279 in the range of $1\text{-}500\ \text{mm s}^{-1}$. c) A Ge-rich stagnant layer is formed due to the diffusion and d) d)
 280 thermocapillary-driven convection within the traveling molten zone, which is shown here only
 281 for at $1\ \text{mm s}^{-1}$. e) Simulated spatial redistribution of the composition in the cross-section and
 282 on the top surface of a laser-written microstripe. An in-plane longitudinal SiGe heterostructure
 283 was formed with a Ge-rich strip core and Si-rich under-cladding. f) Optical microscope image
 284 showing the angle polished cross-section and top facet of a longitudinal SiGe heterostructure
 285 laser-written at $200\ \text{mm s}^{-1}$ for the sake of experimental comparison.

286 The simulation results presented in Figure 1(b) show the spatial redistribution of the Ge
 287 molar fraction x within the laser-processed microstripes at various constant scan speeds. The
 288 laser-induced molten zone (in red colour) travels along the scan direction dragging the Ge-rich
 289 liquid, and solidifies at the trailing edge with a scan-speed-dependent redistribution of the initial
 290 composition $x_0=0.5$. After a short Si-rich transient (blue colour), an indefinitely long steady-
 291 state region emerges with a Ge-rich ($x > 0.5$) strip core (orange) and a Si-rich ($x < 0.5$) under-
 292 cladding. Distribution of the composition in the molten zone is not homogenous as shown in
 293 Figure 1(c), because the thermocapillary convection pushes the liquid radially outwards from
 294 the centre as shown in Figure 1(d), forming a Ge-rich stagnant layer close to the boundary
 295 (darker red), where the flow speed decreases to 0 m s^{-1} from a maximum value of 2.3 m s^{-1} . At
 296 high scan speeds, a build-up of Ge occurs at the trailing edge because of insufficient diffusion-
 297 limited transport to reach complete mixing in the stagnant layer, as in the case for low scan
 298 speeds.

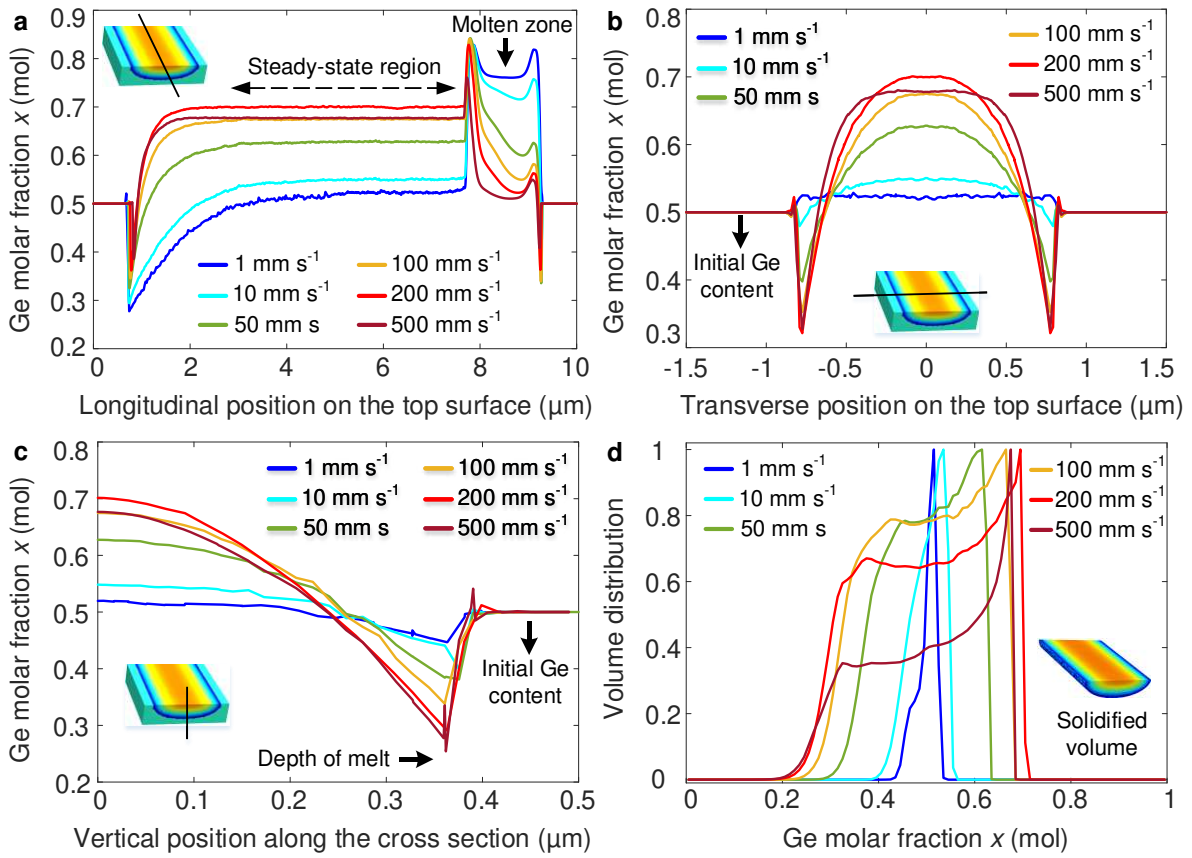


299
 300 **Fig. 2: STEM and EDX analysis of an in-plane laser-written longitudinal SiGe**
 301 **heterostructure at a scan speed of 200 mm s^{-1} .** a) High-angle annular dark-field image
 302 (HAADF) showing the material contrast at the cross-section of the laser-processed region. b)
 303 Simulated result showing SiGe composition at the cross-section for comparison. The image size
 304 was rescaled accordingly to match the beam size used in the experiments. EDX images showing
 305 c) Ge and d) Si spatial distributions at the cross-section.

306 To compare our simulation results with the experiments, a laser-processed SiGe epilayer
307 was cleaved in the middle, and its cleaved edge was angle polished to reveal the cross-section
308 of a longitudinal heterostructure laser-written at a scan speed of 200 mm s^{-1} . The simulated
309 redistribution of the composition on the top surface and in the cross section shown in [Figure](#)
310 [1\(e\)](#), agrees well with the experimental result shown in the optical microscope image given in
311 [Figure 1\(f\)](#). The Ge-rich top surface (yellow) and boundary of the Si-rich cladding (blue) are
312 clearly observable via the natural colour contrast. Additionally, the SiGe microstripe was
313 analysed using STEM with EDX. A high-angle annular dark-field (HAADF) image, which was
314 taken with $14000\times$ magnification of the cross-section at 200 keV , shows the material contrast
315 due to the composition redistribution in the solidified region in [Figure 2\(a\)](#). Our simulated result,
316 which was calculated from the simulation data in [Figure 1\(e\)](#), shows the $\text{Si}_{1-x}\text{Ge}_x$ composition
317 at the cross-section in [Figure 2\(b\)](#). It agrees qualitatively well with the EDX images revealing
318 the spatial redistribution of Ge and Si separately in [Figure 2\(c,d\)](#).

319 The calculated Ge molar fraction profiles along different directions at the top surface
320 and cross-section are given in [Figure 3\(a-c\)](#) for the in-plane longitudinal SiGe heterostructures
321 laser-written at different scan speeds. The increase of the Ge content in the stagnant layer close
322 to the liquid/solid interface can be clearly seen in [Figure 3\(a\)](#). A maximum Ge molar fraction
323 of $x=0.7$ is reached on the top surface in the solidified region for the scan speed of 200 mm s^{-1} .
324 Higher scan speeds result in the levelling off of the Ge composition x , widening the width of
325 the Ge-rich strip core, as shown in [Figure 3\(b\)](#) for the scan speed of 500 mm s^{-1} . The phase-
326 field gradient $\nabla\phi$ has the highest value at the bottom of the molten zone, which increases the
327 effect of phase segregation according to [Eq. \(16\)](#). Therefore, the most Si-rich region in the
328 under-cladding occurs at the bottom, as shown in [Figure 3\(c\)](#). The effect of laser driven phase
329 segregation on the dispersion of the Ge molar fraction can be clearly seen by calculating
330 histograms of the composition within the entire solidified volume in the steady-state region for

331 different scan speeds, as shown in Figure 3(d). These results complement our understanding of
 332 the formation of in-plane longitudinal heterostructures using laser processing.



333
 334 **Fig. 3: Simulation results showing the $\text{Si}_{1-x}\text{Ge}_x$ composition profiles along different**
 335 **directions on various surfaces, and dispersion of the initial composition for scan speeds in**
 336 **the range of 1-500 mms^{-1} .** Inset figures show the surface and direction where the composition
 337 profile was taken. Ge molar fraction $x(r)$ along the **a)** longitudinal and **b)** transverse directions
 338 on the top surface, and **c)** along the vertical direction at the cross-sections of laser-written SiGe
 339 microstrips. **d)** Normalized volume histogram showing the scan-speed-dependent dispersion
 340 of the initial composition $x_0=0.5$ within the whole solidified volume in terms of the Ge molar
 341 fraction. The bin size is $\Delta x=0.01$. Inset shows the solidified volume in the steady-state region,
 342 where the histograms were calculated.

343 The phase-field modelling provides good agreement when compared to the
 344 experimental observations of the scan-speed-dependent Ge redistribution. For example, both
 345 the experimental data given in Figure 1(a) and the simulation results given in Figure 3(b) show
 346 that the widening of the Ge-rich strip core on the top surface occurs as the scan speed increases.

347 Moreover, the simulated redistribution of the composition at the cross-section of the laser-
348 processed region displays similar features compared to the experimental result, as shown in
349 [Figure 2\(b-d\)](#). Our FEM-based approach was not limited by the computer memory (<100 GB),
350 but by the total time (>2 days) required to run the simulations. To reduce the total simulation
351 time significantly, the thermocapillary-driven convection can be neglected, because the absence
352 of the convection (Supplementary [Figure S3](#)) would only result in a slightly higher Ge content
353 ($\Delta x < 0.02$) at the centre of the top surface. This difference is experimentally insignificant, as we
354 showed in our previous work that the achievable compositional resolution is typically on the
355 order of 0.05 mol.²⁶

356 **Modal analysis of in-plane longitudinal SiGe heterostructures, and their application as** 357 **graded-index optical waveguides**

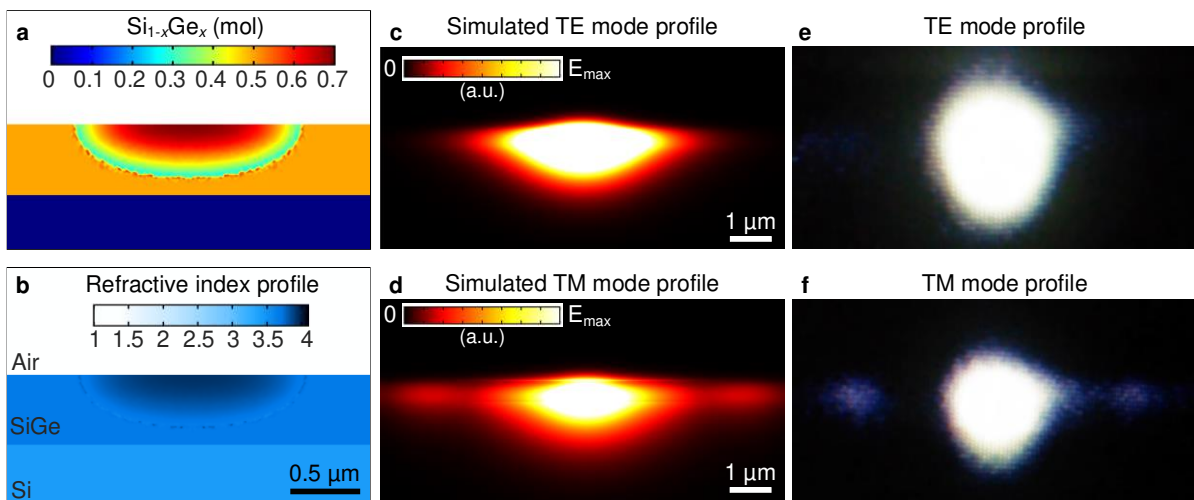
358 Similar to the double heterostructure semiconductor lasers, where optical guiding is achieved
359 in a high index core sandwiched between two lower index claddings, a single longitudinal
360 heterostructure formed with a Ge-rich stripe core and a surrounding Si-rich cladding can
361 provide confinement for light. To illustrate this concept, Maxwell's equations were solved in
362 the frequency domain to calculate the optical modes supported by a longitudinal heterostructure
363 laser-written at a scan speed of 200 mm s^{-1} by a focused beam of $2 \text{ }\mu\text{m}$ in diameter. The 2D Ge
364 molar fraction profile of the laser-written SiGe microstripe, which was obtained by a phase-
365 field simulation, is given in [Figure 4\(a\)](#). The corresponding refractive index profile $n(x)$ at a
366 wavelength of $2 \text{ }\mu\text{m}$ was calculated by using,⁴³

$$367 \quad n(x) = 3.451 + 0.2951x + 0.3419x^2, \quad (43)$$

368 which is a parabolic function of x .

369 The process temperatures, which are high enough to melt the surface, result in biaxial
370 tensile strains within laser-processed SiGe thin films, due to the difference between the thermal
371 expansion coefficients of Ge and Si. A maximum temperature of $1600 \text{ }^\circ\text{C}$ is typically reached
372 during laser melting of the SiGe thin films, resulting in residual strains as high as 0.6%, as

373 demonstrated recently.²⁶ Therefore, photo-elastic effects, which are strain-induced changes in
 374 the refractive index n , need to be considered.⁴⁴ We found that an increase of 3% in the refractive
 375 index within the laser-processed strained region gives the best agreement with the optical
 376 experiments in terms of matching the mode profiles. The resulting refractive index profile $n(x)$,
 377 which includes the photo-elastic effects, is shown in Figure 4(b). The simulated fundamental
 378 mode profiles for the transverse electric (TE) and transverse magnetic (TM) polarized light at
 379 a wavelength of 2 μm are shown in Figure 4(c,d), respectively.



380
 381 **Fig. 4: Laser-written in-plane longitudinal SiGe heterostructures as graded-index optical**
 382 **waveguides. a)** Simulated Ge molar fraction and **b)** calculated refractive index of the cross-
 383 section of a SiGe heterostructure laser-written at a scan speed of 200 mm s^{-1} . Simulated **c)** TE
 384 and **d)** TM polarized mode profiles obtained by modal analysis using the refractive index profile
 385 in **(b)**. IR camera image showing the experimentally captured intensity profiles for the **e)** TE
 386 and **f)** TM polarized modes of light, which was free space coupled into the waveguides using a
 387 fibre laser emitting at 2 μm wavelength.

388 For a proof-of-principle experimental demonstration, we used a 1 cm long SiGe
 389 microstrip that was written using a laser with a spot size of 5 μm at a scan speed of 200 mm s^{-1} .
 390 The end facets were prepared by manual cleaving for optical coupling, and a fibre laser
 391 emitting light at a wavelength of 2 μm was first free space coupled into the SiGe graded-index
 392 waveguide by using a 60 \times objective. The light at the output was then collimated by a 40 \times
 393 objective and imaged by infra-red (IR) camera, which captured the images of the TE and TM

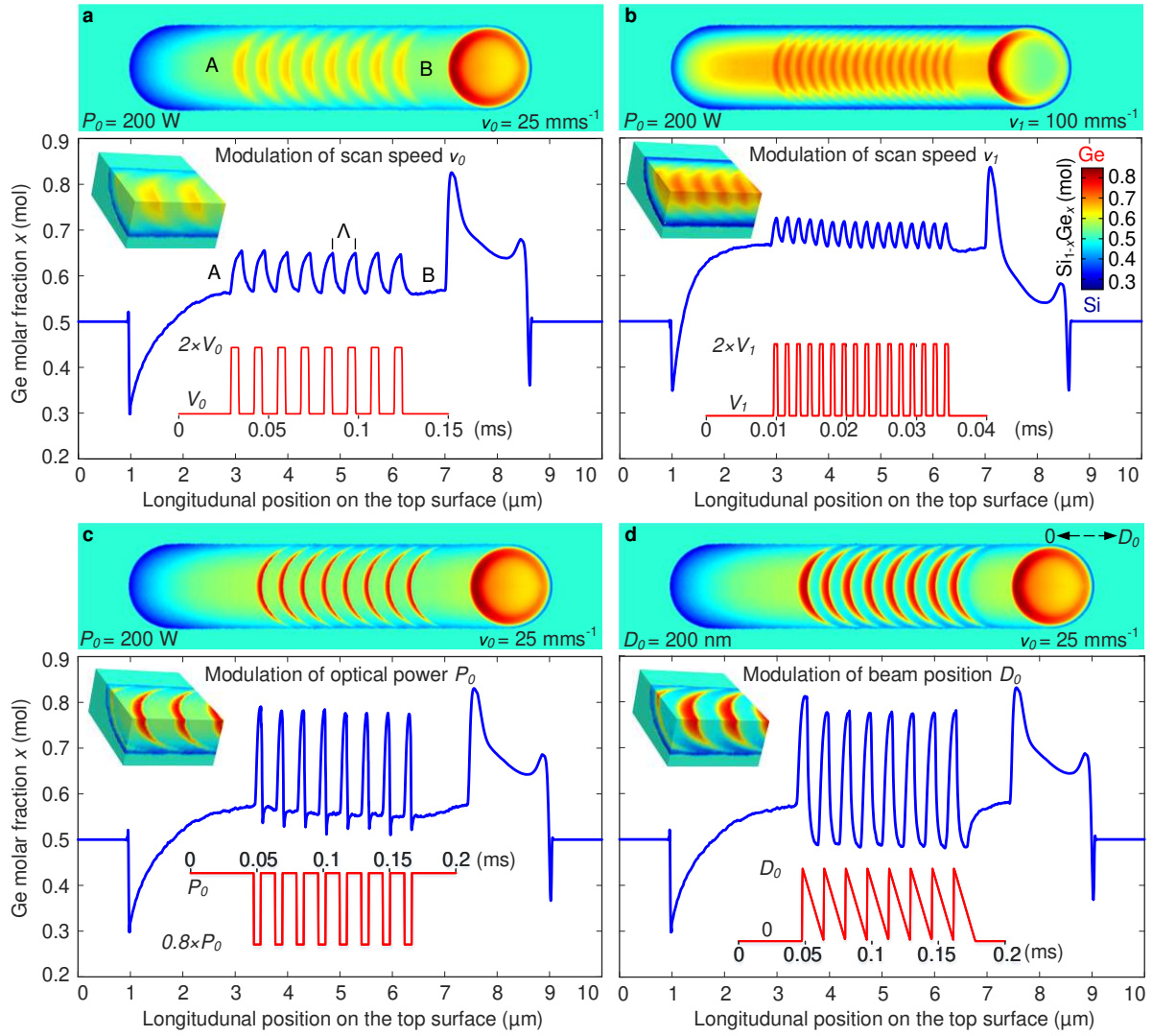
394 polarized modes shown in [Figure 4\(e,f\)](#), respectively. A schematic for the experimental setup
395 used for optical coupling is given in Supplementary [Figure S4](#). In agreement with the optical
396 simulations, we observed that only the fundamental TE and TM polarized modes were guided
397 through these 1 cm long embedded SiGe waveguides at a wavelength of 2 μm . Moreover,
398 optical guiding was observed even for the waveguide written at the lowest scan speed of 0.1
399 mm s^{-1} , where the least compositional separation of Si and Ge occurs within the solidified
400 region. This observation confirms our assumption that the residual tensile strains increase the
401 refractive index in the laser-processed regions to allow for optical guiding. The TM polarized
402 mode was found to be lossy; therefore, it leaks from the strip core decreasing the intensity of
403 the coupled light during propagation. However, the thickness of the grown SiGe epilayer can
404 be increased to obtain a deeper melted region, providing more confinement for the TM
405 polarized mode. Graded-index SiGe waveguides have recently received increased interest for
406 mid-infrared (MIR) applications in integrated photonics,⁴⁵ due both to the low optical losses (1
407 dB cm^{-1}) and their tunable optical properties via compositional engineering.

408 **Simulations of in-plane transverse SiGe superlattices fabricated by modulation of the scan** 409 **speed, optical power, and beam position during laser processing**

410 As the steady-state region within the laser-written microstripes is indefinitely long (depending
411 only on the total scan range), the process parameters can be modulated to create transient effects
412 superimposed on the constant scan speed during laser writing. We first performed simulations
413 with the modulation of the stage scan speed to produce periodic heterostructures in the steady-
414 state region. A 77.6 kHz square wave modulation of the stage scan speed v between 25-50 mm
415 s^{-1} with a duty cycle of 1/3 resulted in a SiGe superlattice with a period of $\Lambda=430$ nm, as shown
416 in [Figure 5\(a\)](#). The resulting periodic composition profile is embedded into the Ge-rich core
417 strip and diminishes close to the surrounding Si-rich cladding (down to a depth of 300 nm), as
418 shown in the inset figure. The composition profile (blue) along the longitudinal axis on the top
419 surface shows the Ge molar fraction, where the DC level is determined by the initial scan speed,

420 as shown in [Figure 3\(a\)](#). It is possible to obtain a higher DC composition level up to the
421 maximum Ge molar fraction of $x=0.7$ by increasing the scan speed; however, this requires
422 application of much higher modulation frequencies to achieve the same superlattice period. To
423 demonstrate a smaller period and a different DC level, we performed a 621.1 kHz modulation
424 of the stage scan speed v between 100-200 mm s⁻¹, which forms a SiGe superlattice with a
425 period of $\Lambda=220$ nm, as shown in [Figure 5\(b\)](#). Although smaller periods down to 100 nm could
426 be achieved, the finiteness of the mesh (minimum 20 nm) limits the resolution of the simulated
427 heterostructures.

428 Modulation of the scan speed by controlling the movement of the stage, where the
429 sample is fixed, might be experimentally limited by the maximum achievable acceleration due
430 to the inertia of the stage mechanism. Much faster translational transients for the laser-induced
431 molten zone can be realized by modulating either the laser power or position of the laser beam
432 using electro-optic modulators and deflectors or acousto-optic scanners, while the stage moves
433 independently at a constant scan speed. We performed 20% modulation of the laser power
434 $P_0=200$ mW with a duty cycle of 1/3 at 61.0 kHz to obtain an in-plane transverse SiGe
435 superlattice with a period of $\Lambda=402$ nm, as shown in [Figure 5\(c\)](#). In this case, we were able to
436 obtain a greater change in the Ge molar fraction in the range of $\Delta x=0.55-0.78$ mol, via the higher
437 acceleration of the solidification boundary when the spot size suddenly shrinks due to the 20%
438 power reduction. Another convenient option for modulation is switching the position of the
439 laser beam back and forth on the sample surface while the stage moves at a constant scan speed.
440 A 61.1 kHz sawtooth modulation of the beam position with a displacement of $D_0=200$ nm
441 resulted in a SiGe superlattice with a period of $\Lambda=410$ nm, as shown in [Figure 5\(d\)](#). Slowing
442 the speed of the beam spot in the return cycle helps to lower the Ge molar fraction down to the
443 initial value of $x_0=0.5$ between the two maxima of the composition. Animated simulation
444 results for modulation of the laser beam position and power are shown in [Supplementary](#)
445 [Movies S1](#) and [S2](#), respectively.



446

447

448

449

450

451

452

453

454

455

456

457

458

459

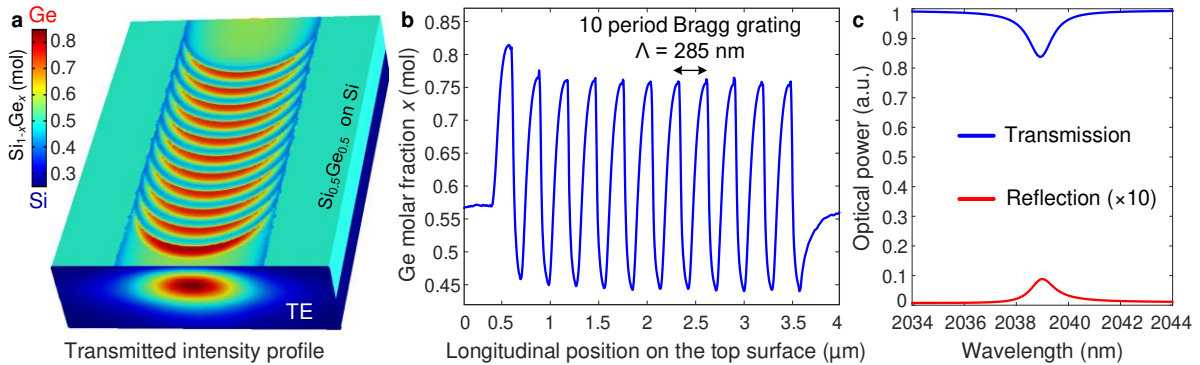
Fig. 5: Laser-written in-plane transverse SiGe superlattices fabricated by sub-millisecond modulation of scan speed, optical power, and beam position. Composition colour maps show the Ge molar fraction x on the top surface of the laser-written microstrips. Inset figures show the periodic composition distributions at the transverse and longitudinal cross-sections to reveal the depth of the modulated regions. Modulated process parameters and resulting composition profiles on the top surface are given in red and blue colours, respectively. All square wave modulations have a duty cycle of 1/3. **a)** A 77.6 kHz square wave modulation of the stage scan speed v between 25-50 mm s^{-1} results in an in-plane SiGe superlattice with a period of $\Lambda=430$ nm. **b)** 621.1 kHz modulation of the stage scan speed v between 100-200 mm s^{-1} forms a SiGe superlattice with a period of $\Lambda=220$ nm. **c)** 61.0 kHz 20% modulation of the laser power $P_0=200$ mW forms a SiGe superlattice with a period of $\Lambda=402$ nm. **d)** 61.1 kHz sawtooth wave modulation of the beam position with a back-and-forth displacement of $D_0=200$ nm forms a SiGe superlattice with a period of $\Lambda=410$ nm.

460 **3D FEM-based optical simulations for transmission and reflection spectra of an in-plane**
 461 **transverse SiGe superlattice as a Bragg grating notch filter**

462 Waveguide Bragg gratings, which consist of alternating layers of materials with different
 463 refractive indices within a waveguide, is one of the basic elements used in integrated photonics
 464 today. Primary methods used to fabricate Bragg gratings are material removal by etching,⁴⁶ and
 465 local refractive index modification induced by ultra-fast lasers.⁴⁷ Laser-written in-plane
 466 transverse SiGe superlattices can be exploited as a waveguide Bragg grating if the pitch size
 467 (period) Λ of the grating satisfies the Bragg condition

$$468 \quad \lambda = 2n_{eff}\Lambda, \quad (28)$$

469 where λ is the wavelength of interest, and n_{eff} is the effective index of the reflected optical mode
 470 in the waveguide.



471
 472 **Fig. 6: Laser-written in-plane transverse SiGe superlattice on a silicon substrate as a**
 473 **waveguide Bragg grating notch filter in the mid-IR regime. a)** Composition colour map
 474 shows the periodic Ge molar fraction x on the top surface of an in-plane transverse SiGe
 475 superlattice written at a stage scan speed of 25 mm s^{-1} , using a sawtooth wave modulation of
 476 the laser beam position. Calculated optical intensity profile of a TE polarized mode is shown as
 477 superimposed on the output facet of the simulated waveguide Bragg grating. **b)** Ge molar
 478 fraction profile as a function of position along the centre line on the top surface showing a 10-
 479 period grating with a pitch size of 285 nm. **c)** Calculated transmission and reflection spectra of
 480 the 10-period SiGe waveguide Bragg grating by 3D FEM-based optical simulations. The
 481 reflection data (red) is magnified 10 times for clarity.

482 We simulated an in-plane transverse SiGe superlattice laser-written at a constant stage
483 scan speed of 25 mm s^{-1} , using a sawtooth modulation of the laser beam position with a
484 displacement D of 200 nm. A 10-period Bragg grating with a pitch size of $\Lambda_0=285 \text{ nm}$ was
485 chosen for a wavelength filtering application at an IR wavelength range around $2 \mu\text{m}$, as shown
486 in [Figure 6\(a\)](#). The total length of the Bragg grating was kept short, due to the computational
487 constraints for the FEM-based optical simulations in 3D. However, to increase the coupling
488 between propagating and counter-propagating optical modes in such a short waveguide Bragg
489 grating, we ensured that the maximum refractive index modulation was achieved in the periodic
490 composition profile ($\Delta x=0.45-0.75$), as shown in [Figure 6\(b\)](#). The calculated transmission and
491 reflection spectra of the 10-period waveguide Bragg grating are shown in [Figure 6\(c\)](#). Further
492 details regarding implementation of the optical simulations are given in the [Methods](#).

493 A dip in the transmission spectrum was observed at a wavelength of 2038.9 nm for the
494 reflected TE mode with an effective index of $n_{eff} = 3.5244$. By using the Bragg condition in [Eq.](#)
495 [\(28\)](#), we found that this corresponds to a pitch size Λ of 289.3 nm, which is close to the
496 simulated pitch size $\Lambda_0 = 285 \text{ nm}$. A slight mismatch in the pitch is expected due to the coarser
497 size of the mesh (40 nm) used for the optical simulations. Additionally, we noticed that the
498 reflection was suppressed, which is desired for a notch filter application. The reduction in the
499 reflection is common for single mode waveguides with asymmetric gratings, like a tilted fibre
500 Bragg grating, which couple the reflected light into higher order lossy modes. As our laser-
501 written waveguides support only the fundamental TE mode at a wavelength of 2000 nm, we
502 expect high losses for the reflected higher order mode. A waveguide Bragg grating with a high
503 number of periods (>1000) and a longer total length ($>300 \mu\text{m}$) would be straightforward to
504 fabricate to achieve better rejection ratios in the stop band and thus could find ready use in
505 integrated photonics applications.

506

507

508 **DISCUSSION**

509 Laser-driven phase segregation in alloy epilayers allows for achieving Ge concentrations
510 remarkably higher ($x=0.7$) and lower ($x=0.25$) than the initial composition $x_0=0.5$ within the
511 solidified regions. The laser-processed region consists of a Ge-rich core and a Si-rich under-
512 cladding, forming an in-plane longitudinal heterostructure. At high scan speeds, Ge
513 accumulates at the trailing edge of the annular stagnant layer, which is formed by the
514 thermocapillary convection within the laser-induced molten zone. The solidified region
515 becomes compositionally more uniform and wider on the top surface after a high scan speed,
516 at which a maximum Ge concentration is reached. To obtain higher Ge concentrations, either
517 SiGe epilayers with an initially higher Ge content or a multi-scan approach can be used.

518 The transient effects superimposed on the constant stage scan speed via programmable
519 modulation of the laser processing parameters allows for fabrication of versatile in-plane
520 periodic heterostructures with interfaces transverse to the scan direction and in the morphology
521 of the laser beam. Therefore, laser beam shapers can be used to obtain non-circular beam shapes
522 such as square, super-ellipse or V-shape. For example, in-plane traverse heterostructures with
523 straight interfaces perpendicular to the scan direction could be written using a rectangular-
524 shaped laser beam. Although the transverse size of the heterostructure is determined by the size
525 of the laser beam spot, the pitch of the periodic heterostructures are not diffraction-limited. This
526 is because it is not the spot area,⁴⁸ but the displacement of the 2D liquid/solid interface in the
527 scan direction that determines the pitch size, which in principle can be as small as the resolution
528 of the beam scanner/deflector allows. Moreover, laser-driven phase segregation with
529 modulation of the process parameters could be applied to fabricate in-plane heterostructures in
530 other pseudo-binary systems, such as metal alloys (Ni–Cu), ternary alloys of group III-V
531 semiconductors ($\text{Al}_x\text{Ga}_{1-x}\text{As}$), quaternary alloys of transition metal dichalcogenides
532 ($\text{Mo}_x\text{W}_{1-x}\text{S}_y\text{Se}_{1-y}$),¹³ and ceramics ($\text{Al}_2\text{O}_3\text{--Cr}_2\text{O}_3$), which have a miscibility gap in their phase

533 diagrams similar to that of SiGe. Finally, other thermal sources of directed energy, such e-
534 beams, could be used to melt the surface and to induce similar in-plane heterostructures.

535 In conclusion, we have introduced a concept for direct laser writing of in-plane
536 heterostructures and superlattices within SiGe epilayers, controlling the steady-state and
537 transient effects during non-dendritic solidification by modulating the laser scan speed, optical
538 power, and beam position. 3D FEM-based non-isothermal phase-field simulations including
539 the effects of laser-induced thermocapillary convection were carried out to investigate the
540 formation of in-plane heterostructures with longitudinal and transverse interfaces. We also
541 provided experimental support for laser-driven phase segregation in epitaxially grown $\text{Si}_{0.5}\text{Ge}_{0.5}$
542 films, and demonstrated optical coupling into in-plane longitudinal SiGe heterostructures,
543 which can function as graded-index optical waveguides in a wavelength range of 2-8 μm .
544 Another photonic application was demonstrated by calculating the transmission and reflection
545 of a waveguide Bragg grating based on in-plane transverse SiGe superlattices with a period of
546 285 nm. On-chip, post-process laser writing of in-plane nanoscale heterostructures and
547 superlattices within epilayers of semiconductor alloys without the strain and lattice matching
548 limitations could pave the way for new device applications in the fields of microelectronics,
549 optoelectronics, and photonics.

550 **METHODS**

551 **Implementation of 3D FEM-based phase-field simulations for laser processing**

552 We used the IRIDIS-5 supercomputer (1 node with 40 cores and 192 GB memory) in the
553 University of Southampton to run simulations in 3D with a finite element analysis software
554 (COMSOL Multiphysics 5.5). Time dependent Navier-Stokes equations, which are fully
555 coupled with the heat transport equation in [Eq. \(24\)](#), were solved using the generalized
556 minimum residual iterative solver (GMRES) with an algebraic multigrid preconditioner (AMG).
557 We also accounted for cooling of the top surface of the laser-processed SiGe epilayer, due to
558 the air convection and surface-to-ambient radiation, using boundary conditions. The

559 convection-diffusion-segregation equation in Eq. (16), which is coupled to the Navier-Stokes
560 and heat transport equations, was solved in a segregated way using a parallel sparse direct solver
561 (PARDISO). Time discretization was done using the backwards differentiation formula (BDF).
562 The minimum mesh size was taken as 20 nm to resolve the thickness of the solid/liquid interface.
563 To confirm conservation of Ge content in the $\text{Si}_{1-x}\text{Ge}_x$ epilayer, we calculated volume average
564 of x in the total simulation volume V_{SiGe} , which satisfied the mass conservation constraint
565 $\int x(\vec{r}, t) dV / V_{\text{SiGe}} = x_0$ during simulations. On the other hand, the instantaneous value of the
566 Ge molar fraction $x(\vec{r}, t)$ was also monitored to ensure that it always stays in the range $0 < x <$
567 1. All simulation parameters are given in Supplementary Table S1.

568 **Implementation of FEM-based optical simulations for photonic devices**

569 We used the COMSOL wave optics module for modal analysis of the graded-index waveguides
570 and waveguide Bragg gratings. The fundamental optical modes were found by solving the
571 vector Helmholtz equation, using a multi-frontal massively parallel sparse direct solver
572 (MUMPS). The transmission and reflection spectra of the laser-written SiGe waveguide Bragg
573 grating in the wavelength range of 2030-2050 nm were calculated from the scattering matrix s_{ij}
574 elements found by the 3D FEM-based optical simulations with a wavelength step of $\Delta\lambda=0.1$ nm.

575 **DATA AVAILABILITY**

576 The datasets generated during the current study are available in the University of Southampton
577 Institutional Research Repository at <https://doi.org/10.5258/SOTON/DXXXX>.

578 **ACKNOWLEDGEMENTS**

579 The authors acknowledge the use of the IRIDIS High-Performance Computing Facility at the
580 University of Southampton, and support of the Engineering and Physical Sciences Research
581 Council (EPSRC) (EP/P000940/1 and EP/N013247/1) for the completion of this work.

582 **AUTHOR CONTRIBUTIONS**

583 O.A. and A.C.P. conceived the research. O.A. conducted the simulations and theoretical
584 calculations. Y.Y. and M.K. prepared the epitaxially grown SiGe/Si samples and conducted

585 STEM/EDX analysis. O.A. performed the laser processing of the SiGe samples, their imaging
586 by optical microscopy, and optical coupling experiments for the laser-written waveguides. O.A.
587 and A.C.P. interpreted the results and wrote the manuscript. All authors contributed to the
588 discussion and review.

589 **ADDITIONAL INFORMATION**

590 **Supplementary information** accompanies the paper.

591 **Competing interest:** The authors declare no competing interests.

592 **REFERENCES**

- 593 [1] Alferov, Z. I. Nobel Lecture: The double heterostructure concept and its applications in
594 physics, electronics, and technology. *Rev. Mod. Phys.* **73**, 767–782 (2001).
- 595 [2] Paul, D. J. Si/SiGe heterostructures: from material and physics to devices and circuits.
596 *Semicond. Sci. Technol.* **19**, R75–R108 (2004).
- 597 [3] Paul, D. J. The progress towards terahertz quantum cascade lasers on silicon substrates.
598 *Laser Photonics Rev.* **4**, 610–632 (2010).
- 599 [4] Bhattacharya, P. K. & Dutta, N. K. Quantum well optical devices and materials. *Annu. Rev.*
600 *Mater. Sci.* **23**, 79–123 (1993).
- 601 [5] Tournié, E. & Trampert, A. MBE growth and interface formation of compound
602 semiconductor heterostructures for optoelectronics. *Phys. Stat. Sol. (b)* **244**, 2683–2696 (2007).
- 603 [6] Cai, Z., Liu, B., Zou, X. & Cheng, H.-M. Chemical vapor deposition growth and
604 applications of two-dimensional materials and their heterostructures. *Chem. Rev.* **118**,
605 6091–6133 (2018).
- 606 [7] Isa, F. et al. Highly mismatched, dislocation-free SiGe/Si heterostructures. *Adv. Mater.* **28**,
607 884–888 (2016).
- 608 [8] Li, H., Wang, X., Zhu, X., Duan, X. & Pan, A. Composition modulation in one-dimensional
609 and two-dimensional chalcogenide semiconductor nanostructures. *Chem. Soc. Rev.* **47**, 7504–
610 7521 (2018).

- 611 [9] Zhang, Z., Chen, P., Duan, X., Zang, K., Luo, J. & Duan, X. Robust epitaxial growth of
612 two-dimensional heterostructures, multiheterostructures, and superlattices. *Science* **357**, 788–
613 792 (2017).
- 614 [10] Wu, Y., Fan, R. & Yang, P. Block-by-block growth of single-crystalline Si/SiGe
615 superlattice nanowires. *Nano Lett.* **2**, 83–86, (2002).
- 616 [11] Fang, X. et al. Heterostructures and superlattices in one-dimensional nanoscale
617 semiconductors. *J. Mater. Chem.* **19**, 5683–5689 (2009).
- 618 [12] Chueh, Y.-L. et al. Nanoscale structural engineering via phase segregation: Au-Ge system.
619 *Nano Lett.* **10**, 393-397 (2010).
- 620 [13] Susarla, S. et al. Thermally induced 2D alloy-heterostructure transformation in quaternary
621 alloys. *Adv. Mater.* **30**, 1804218 (2018).
- 622 [14] Wu, M. et al. Detecting lateral composition modulation in dilute Ga(As,Bi) epilayers.
623 *Nanotechnology* **26**, 425701 (2015).
- 624 [15] Conti M. Interface dynamics, instabilities, and solute bands in rapid directional
625 solidification. *Phys. Rev. E* **58**, 2071–2078 (1998).
- 626 [16] Yamamoto, Y. et al. Ge/SiGe multiple quantum well fabrication by reduced-pressure
627 chemical vapor deposition. *Jpn. J. Appl. Phys.* **59**, SGGK10 (2020).
- 628 [17] Kurz, W. & Fisher, D. J. in *Fundamentals of Solidification* Ch. 3 (Trans Tech Publications,
629 1992).
- 630 [18] Miller, W., Abrosimov, N., Rasin, I. & Borissova, D. Cellular growth of Ge_{1-x}Si_x single
631 crystals. *J. Cryst. Growth* **310**, 1405–1409 (2008).
- 632 [19] Gotoh, R. et al. Formation mechanism of cellular structures during unidirectional growth
633 of binary semiconductor Si-rich SiGe materials. *Appl. Phys. Lett.* **100**, 021903 (2012).
- 634 [20] Mokhtari, M. et al. Instability of crystal/melt interface in Si-rich SiGe. *J. Appl. Phys.* **124**,
635 085104 (2018).

- 636 [21] Weizman, M., Nickel, N. H., Sieber, I. & Yan, B. Successive segregation in laser-
637 crystallized poly-SiGe thin films. *J. Non-Cryst. Solids* **352**, 1259–1262 (2006).
- 638 [22] Kitahara, K., Hirose, K., Suzuki, J., Kondo, K. & Hara, A. Growth of quasi-single-crystal
639 silicon-germanium thin films on glass substrates by continuous wave laser lateral crystallization.
640 *Jpn. J. Appl. Phys.* **50**, 115501 (2011).
- 641 [23] Gaiduk, P. I. & Prakopyeu, S. L. in *Subsecond Annealing of Advanced Materials* (eds
642 Skorupa, W. & Schmidt, H.) Ch. 5 (Springer, 2014).
- 643 [24] Ong, C. Y., Pey, K. L., Li, X., Wang, X. C., Ng, C. M. & Chan, L. Laser annealing induced
644 high Ge concentration epitaxial SiGe layer in $\text{Si}_{1-x}\text{Ge}_x$ virtual substrate. *Appl. Phys. Lett.* **93**,
645 041112 (2008).
- 646 [25] Dagault, L. et al. Impact of UV nanosecond laser annealing on composition and strain of
647 undoped $\text{Si}_{0.8}\text{Ge}_{0.2}$ epitaxial layers. *ECS J. Solid State Sci. Technol.* **8**, P202-P208 (2019).
- 648 [26] Aktas, O. et al. Laser-driven phase segregation and tailoring of compositionally graded
649 microstructures in Si–Ge nanoscale thin films. *ACS Appl. Mater. Interfaces* **12**, 9457–9467
650 (2020).
- 651 [27] Tiller, W. A., Jackson, K. A., Rutter, J. W. & Chalmers, B. The redistribution of solute
652 atoms during the solidification of metals. *Acta Metall.* **1**, 428–437 (1953).
- 653 [28] Coucheron, D. A. et al. Laser recrystallization and inscription of compositional
654 microstructures in crystalline SiGe-core fibres. *Nat. Commun.* **7**, 13265 (2016).
- 655 [29] Chen, L.-Q. Phase field models for microstructure evolution. *Annu. Rev. Mater. Res.* **32**,
656 113–140 (2002).
- 657 [30] Warren, J. A. & Boettinger, W. J. Prediction of dendritic growth and microsegregation
658 patterns in a binary alloy using the phase-field method. *Acta Metall. Mater.* **43**, 689–703 (1995).
- 659 [31] Moelans, N., Blanpain, B. & Wollants, P. An introduction to phase-field modeling of
660 microstructure evolution. *Comput. Coupling Phase Diagrams Thermochem.* **32**, 268–294
661 (2008).

- 662 [32] Lin, H. K., Chen, H. Y. & Lan, C. W. Adaptive phase field modeling of morphological
663 instability and facet formation during directional solidification of SiGe alloys. *J. Cryst. Growth*
664 **385**, 44–48 (2014).
- 665 [33] Lockwood, D. J. et al. Si/SiGe heterointerfaces in one-, two-, and three-dimensional
666 nanostructures: Their impact on SiGe light emission. *Front. Mater.* **3**, 12 (2016).
- 667 [34] Ballabio, A. et al. Ge/SiGe parabolic quantum wells. *J. Phys. D: Appl. Phys.* **52**, 415105
668 (2019).
- 669 [35] Boettinger, W. J., Warren, J. A., Beckermann, C. & Karma, A. Phase-field simulations of
670 solidification. *Annu. Rev. Mater. Res.* **32**, 163–94 (2002).
- 671 [36] De Oliveira, M. J. in *Equilibrium Thermodynamics* (eds Rhodes, W. T., Stanley, H. E. &
672 Needs, R.) Ch. 10 (Springer, 2013).
- 673 [37] Bi, Z. & Sekerka, R. F. Phase-field model of solidification of a binary alloy. *Physica A*
674 **261**, 95–106 (1998).
- 675 [38] Ricci, E. et al. Surface tension and density of Si-Ge melts. *J. Chem. Phys.* **140**, 214704
676 (2014).
- 677 [39] Siquieri, R. & Emmerich, H. Phase-field investigation of microstructure evolution under
678 the influence of convection. *Philos. Mag.* **91**, 45-73 (2010).
- 679 [40] Steinbach, I. Phase-field models in materials science. *Modelling Simul. Mater. Sci. Eng.*
680 **17**, 073001 (2009).
- 681 [41] Chan, C. L., Mazumder, J. & Chen, M. M. Effect of surface tension gradient driven
682 convection in a laser melt pool: Three-dimensional perturbation model. *J. Appl. Phys.* **64**, 6166–
683 6174 (1988).
- 684 [42] Zhang, Q. Z. et al. Numerical investigation on selective emitter formation by laser doping
685 for phosphorous-doped silicon solar cells. *J. Laser Appl.* **29**, 022003 (2017).
- 686 [43] Barritault, P. et al. Mlines characterization of the refractive index profile of SiGe gradient
687 waveguides at 2.15 μm . *Opt. Express* **21**, 11506–11515 (2013).

- 688 [44] Rho, H., Jackson, H. E. & Weiss, B. L. Mapping of local stress distributions in SiGe/Si
689 optical channel waveguide. *J. Appl. Phys.* **90**, 276–282 (2001).
- 690 [45] Brun, M. et al. Low loss SiGe graded index waveguides for mid-IR applications. *Opt.*
691 *Express* **22**, 508–518 (2014).
- 692 [46] Liu, Q. et al. On-chip Bragg grating waveguides and Fabry-Perot resonators for long-wave
693 infrared operation up to 8.4 μm . *Opt. Express* **26**, 34366–34372 (2018).
- 694 [47] Ams, M., Dekker, P., Gross, S. & Withford, M. J. Fabricating waveguide Bragg gratings
695 (WBGs) in bulk materials using ultrashort laser pulses. *Nanophotonics* **6**, 743–763 (2017).
- 696 [48] Igo, J., Gabel, M., Yu, Z.-G., Yang, L. & Gu, Y. Photodefined in-plane heterostructures in
697 two-dimensional In_2Se_3 nanolayers for ultrathin photodiodes. *ACS Appl. Nano Mater.* **2**,
698 6774–6782 (2019).

Figures

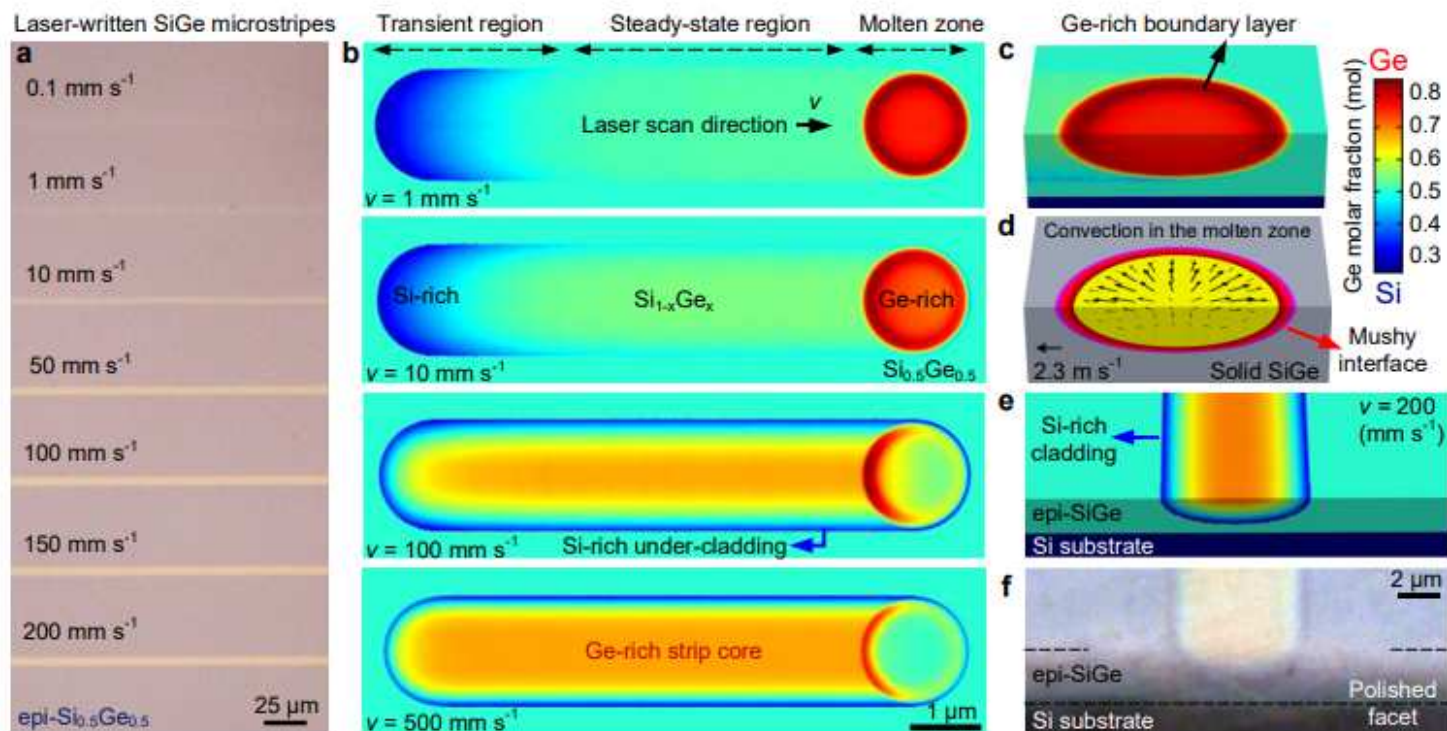


Figure 1

[Please see the manuscript file to view the figure caption.]

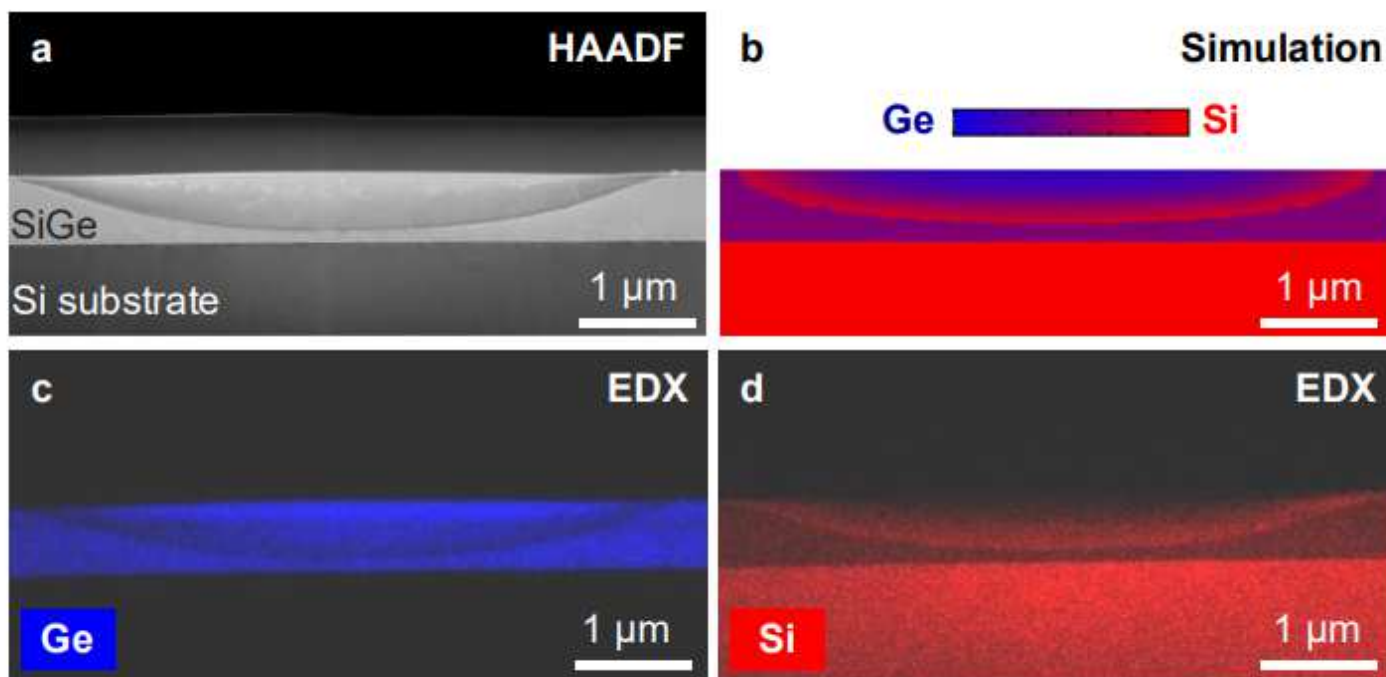


Figure 2

[Please see the manuscript file to view the figure caption.]

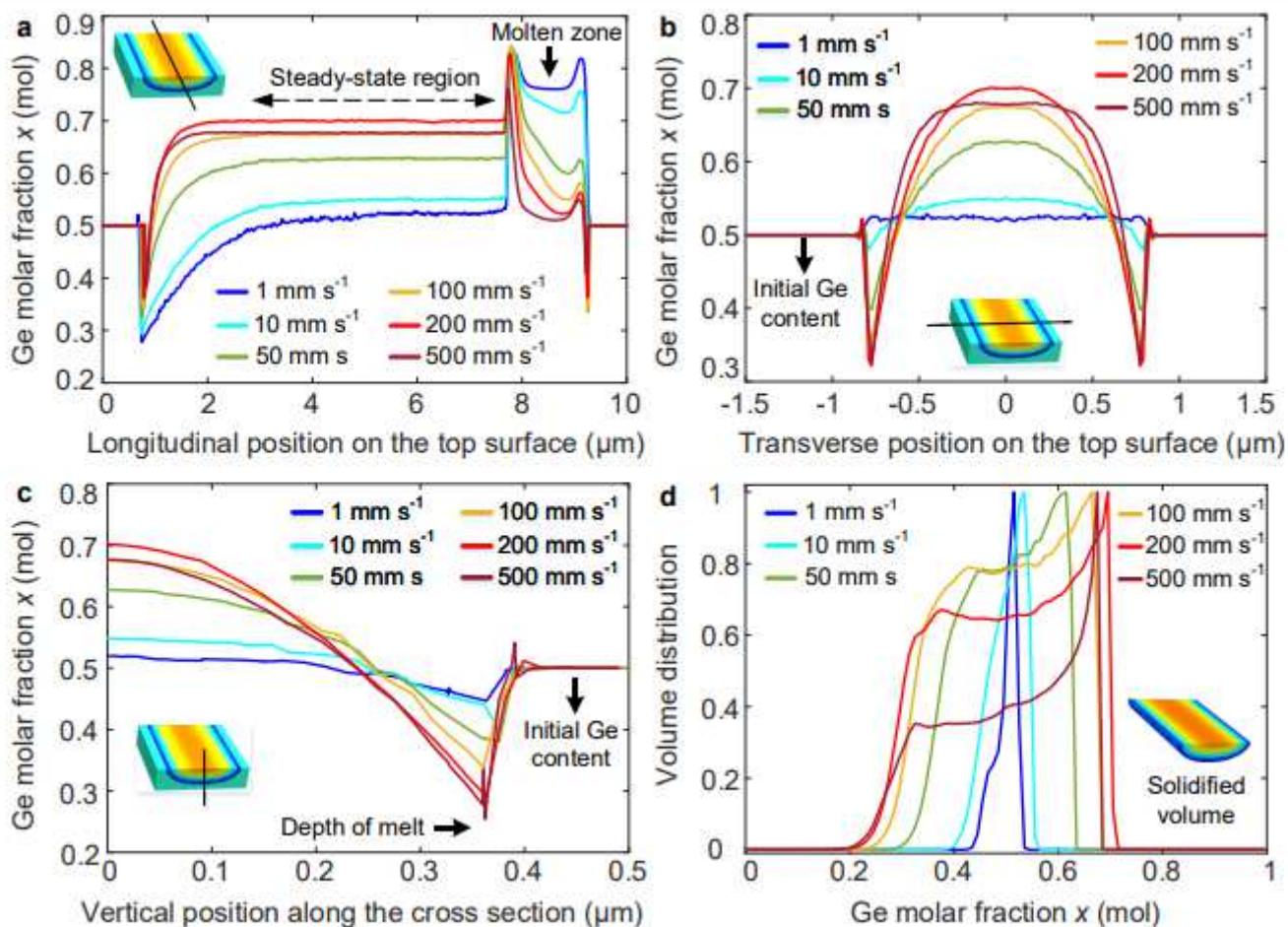


Figure 3

[Please see the manuscript file to view the figure caption.]

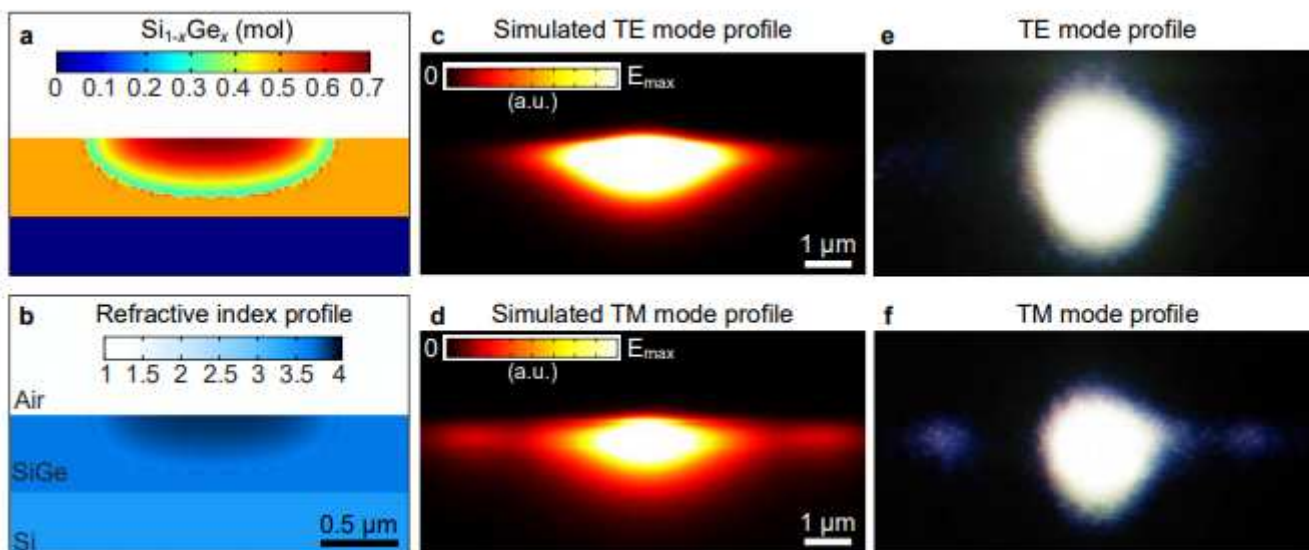


Figure 4

[Please see the manuscript file to view the figure caption.]

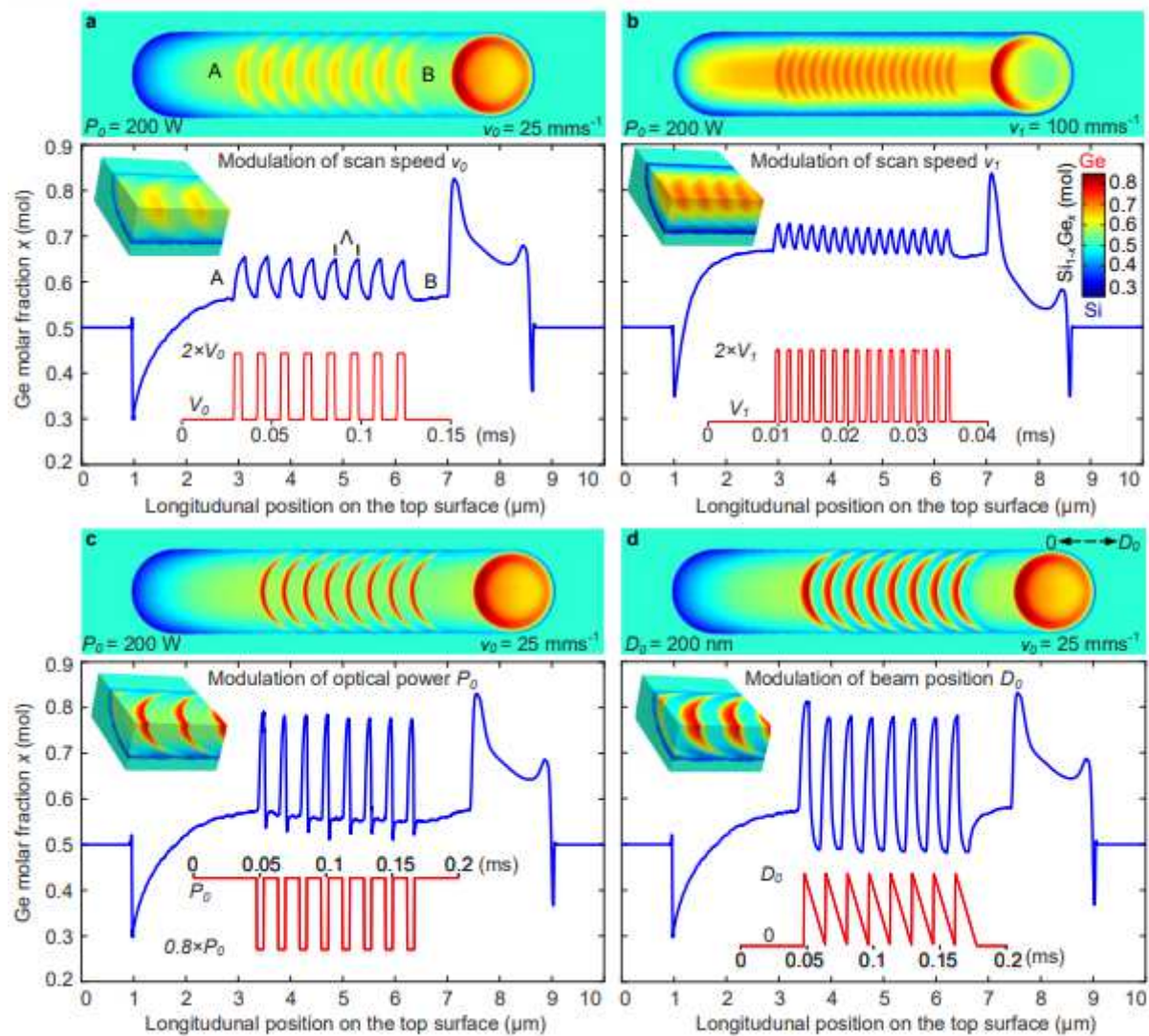


Figure 5

[Please see the manuscript file to view the figure caption.]

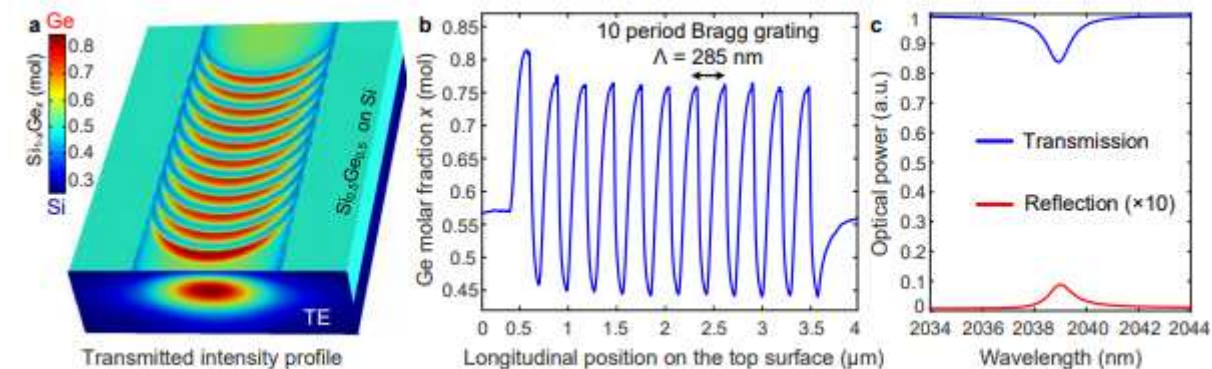


Figure 6

[Please see the manuscript file to view the figure caption.]

Supplementary Files

This is a list of supplementary files associated with this preprint. Click to download.

- [SupplementaryMovieS1.gif](#)
- [SupplementaryMovieS2.gif](#)
- [SupplementaryInformationV5.pdf](#)